PxdA interacts with the DipA phosphatase to regulate peroxisome hitchhiking on early endosomes

John Salogiannis[a,b,†], Jenna R. Christensen[a,†], Livia D. Songster[a,c], Adriana Aguilar-Maldonado[a], Nandini Shukla[d,e,‡], and Samara L. Reck-Peterson[a,b,c,*]

[a]Department of Cellular and Molecular Medicine and [c]Division of Biological Sciences, Cell and Developmental Biology Section, University of California, San Diego, La Jolla, CA 92093; [b]Howard Hughes Medical Institute, Chevy Chase, MD 20815; [d]The Ohio State Biochemistry Program and; [e]Department of Molecular Genetics, The Ohio State University, Columbus, OH 043210

ABSTRACT **In canonical microtubule-based transport, adaptor proteins link cargoes to dynein and kinesin motors. Recently, an alternative mode of transport known as "hitchhiking" was discovered, where cargoes achieve motility by hitching a ride on already-motile cargoes, rather than attaching to a motor protein. Hitchhiking has been best studied in two filamentous fungi, *Aspergillus nidulans* and *Ustilago maydis.* In *U. maydis,* ribonucleoprotein complexes, peroxisomes, lipid droplets (LDs), and endoplasmic reticulum hitchhike on early endosomes (EEs). In *A. nidulans,* peroxisomes hitchhike using a putative molecular linker, peroxisome distribution mutant A (PxdA), which associates with EEs. However, whether other organelles use PxdA to hitchhike on EEs is unclear, as are the molecular mechanisms that regulate hitchhiking. Here we find that the proper distribution of LDs, mitochondria, and preautophagosomes do not require PxdA, suggesting that PxdA is a peroxisome-specific molecular linker. We identify two new *pxdA* alleles, including a point mutation (R2044P) that disrupts PxdA's ability to associate with EEs and reduces peroxisome movement. We also identify a novel regulator of peroxisome hitchhiking, the phosphatase DipA. DipA colocalizes with EEs and its association with EEs relies on PxdA. Together, our data suggest that PxdA and the DipA phosphatase are specific regulators of peroxisome hitchhiking on EEs.**

Monitoring Editor
Anne Spang
University of Basel

Received: Aug 27, 2020
Revised: Jan 7, 2021
Accepted: Jan 15, 2021

INTRODUCTION

The precise spatiotemporal distribution of cargoes is critical for cell growth, maturation, and maintenance. Long-distance movement of cargoes including vesicles, organelles, mRNAs, and macromolecular complexes is driven by molecular motor-dependent transport on microtubules (Vale, 2003; Hirokawa *et al.*, 2009; Cianfrocco *et al.*, 2015; Reck-Peterson *et al.*, 2018). Microtubules are polarized structures with their "plus" ends located near the cell periphery and "minus" ends embedded near the nucleus at microtubule-organizing centers. In mammalian cells, dozens of kinesin motors carry cargoes long distances toward the cell periphery, but a single cytoplasmic-dynein-1 ("dynein" here) transports cargoes toward the cell center (Vale, 2003; Hirokawa *et al.*, 2009; Cianfrocco *et al.*, 2015; Reck-Peterson *et al.*, 2018).

The filamentous fungus *Aspergillus nidulans* is an ideal model system to study mechanisms of microtubule-based transport (Egan *et al.*, 2012a; Peñalva *et al.*, 2012). Similar to mammalian cells, but unlike budding yeast, *A. nidulans* uses microtubule-based transport for the distribution and long-distance movement of cargoes within its long hyphae. It encodes one dynein, *nudA*, and three cargo-carrying kinesins including the kinesin-1 *kinA* and two kinesin-3's, *uncA* and *uncB* (Zekert and Fischer, 2009; Egan *et al.*, 2012a;

This article was published online ahead of print in MBoC in Press (http://www.molbiolcell.org/cgi/doi/10.1091/mbc.E20-08-0559) on January 21, 2021.

†These authors contributed equally to this work.

Author contributions: J.S., J.R.C., and S.L.R.-P. devised the experiments. J.S., J.R.C., and L.S. performed experiments with help from A.A.-M. N.S. shared unpublished findings about DipA. SL.R.-P. supervised the research. J.S., J.R.C., and S.L.R.-P. wrote and edited the manuscript, with feedback from N.S. and L.S.

‡Present address: Section of Molecular Biology, Division of Biological Sciences, University of California, San Diego, La Jolla, CA 92093.

*Address correspondence to: Samara L. Reck-Peterson (sreckpeterson@ucsd.edu).

Abbreviations used: EE, early endosome; LD, lipid droplet; PxdA, peroxisome distribution mutant A.

Peñalva *et al.*, 2012). Microtubules near the hyphal tips are uniformly polarized with their plus ends oriented tip-ward (Egan *et al.*, 2012b), making the directionality of cargo transport and their motors easy to identify. We and others have exploited these features by performing forward genetic screens to identify regulators of microtubule-based transport (Morris, 1975; Xiang *et al.*, 1994, 1999; Downes *et al.*, 2014; Tan *et al.*, 2014; Yao *et al.*, 2014, 2015; Zhang *et al.*, 2014).

The current dogma of microtubule-based transport is that distinct cargoes directly recruit molecular motors via adaptors (Fu and Holzbaur, 2014; Reck-Peterson *et al.*, 2018; Cross and Dodding, 2019). For example, in mammalian cells, members of the Bicaudal-D and Hook cargo adaptor families link dynein and some kinesins to cargo (Hirokawa *et al.*, 2009; Splinter *et al.*, 2010; Bielska *et al.*, 2014; Hoogenraad and Akhmanova, 2016; Reck-Peterson *et al.*, 2018; Cross and Dodding, 2019; Kendrick *et al.*, 2019; Siddiqui *et al.*, 2019). Altogether, there are dozens of different cargo adaptors that link dynein and kinesin to their cargoes in mammalian cells. On the other hand, there are relatively few cargo adaptors in filamentous fungi. A single homologue from the Hook family (HookA in *A. nidulans* and Hok1 in *Ustilago maydis*) is the only characterized cargo adaptor for microtubule-based motors in filamentous fungi (Bielska *et al.*, 2014; Zhang *et al.*, 2014). Hook proteins are one part of the FHF complex (Xu *et al.*, 2008; Guo *et al.*, 2016), composed of Fts, Hook, and Fts-Hook-interacting protein, which links dynein to early endosomes (EEs) via the small GTPase Rab5/RabA in *A. nidulans* (Yao *et al.*, 2014). In both *A. nidulans* and *U. maydis*, EEs are the best-characterized microtubule-based cargo (Wedlich-Söldner *et al.*, 2002; Lenz *et al.*, 2006; Abenza *et al.*, 2009). However, many other cargoes are moved and distributed along the hyphal axis (Egan *et al.*, 2012a).

How these fungi are capable of properly distributing many cargoes despite having few genetically encoded motors and adaptors is unknown. Recently, a noncanonical mechanism of transport termed "hitchhiking" was discovered (Baumann *et al.*, 2012, 2014; Higuchi *et al.*, 2014; Guimaraes *et al.*, 2015; Salogiannis *et al.*, 2016). A hitchhiking cargo, rather than connecting directly to an adaptor-motor complex, instead achieves motility by attaching itself to another motile-competent cargo (Salogiannis and Reck-Peterson, 2017). Hitchhiking represents a mechanism that could be employed to move many cargoes by a small number of motor-bound cargoes in organisms with few genetically encoded motors and cargo adaptors (Lin *et al.*, 2016; Mogre *et al.*, 2020).

A number of cargoes have been shown to exhibit hitchhiking-like behaviors in different organisms and contexts. In *Saccharomyces cerevisiae*, mammalian neurons, and *U. maydis*, ribonucleoprotein complexes are tethered to and cotransported with different membrane-bound compartments (Göhre *et al.*, 2012; Jansen *et al.*, 2014; Haag *et al.*, 2015; Cioni *et al.*, 2019; Liao *et al.*, 2019). In *U. maydis*, polysomes associate with the RNA-binding protein Rrm4, which interacts with the EE-associated protein Upa1 (Pohlmann *et al.*, 2015). Membrane-bound organelles, including peroxisomes, also hitchhike on motile EEs in both *U. maydis* and *A. nidulans* (Guimaraes *et al.*, 2015; Salogiannis *et al.*, 2016). Using a genetic screen in *A. nidulans*, we previously identified the EE-associated protein PxdA as a critical mediator of peroxisome hitchhiking (Salogiannis *et al.*, 2016). However, how PxdA links peroxisomes to motile EEs and whether other proteins are involved remain unclear. In *U. maydis,* LDs and the endoplasmic reticulum, as well as peroxisomes, hitchhike on EEs (Guimaraes *et al.*, 2015), although *U. maydis* lacks a PxdA homologue (Steinberg, 2016). Recently, mRNAs, peroxisomes and the endoplasmic reticulum have also been shown to hitchhike on endolysosomal membranes in mammalian cells (Guo *et al.*, 2018; Liao *et al.*, 2019; Spits *et al.*, 2021).

Here, we took a three-pronged approach to further determine the mechanism and role of hitchhiking in *A. nidulans*. First, we screened other organelles including mitochondria, preautophagosomes, and LDs and found that PxdA was not required for their proper distribution, suggesting that PxdA is a specific regulator of peroxisomes. In contrast to *U. maydis*, we found that the movement and distribution of LDs was also independent of HookA. Second, we returned to our initial screen (Tan *et al.*, 2014) that identified PxdA and identified two new PxdA alleles, one of which is a point mutation (R2044P) that disrupts the association of PxdA with EEs. Third, we performed immunoprecipitation followed by mass spectrometry and identified the DenA/Den1 phosphatase DipA as a PxdA interacting protein. We showed that DipA is recruited to EEs in a PxdA-dependent manner and is required for peroxisome motility. Our data suggest that PxdA and the DipA phosphatase regulate peroxisome hitchhiking on EEs in the filamentous fungi *A. nidulans*.

RESULTS

LDs move independently of PxdA and EEs in *Aspergillus*

We sought to determine whether other organelles require PxdA for their proper distribution along *A. nidulans* hyphae. To accomplish this, we fluorescently tagged the endogenous copies of Atg8, Tom20, and Erg6 to visualize preautophagosomes (Pinar *et al.*, 2013), mitochondria, and LDs, respectively. To quantify organelle distribution in wild-type (WT) and *pxdA*Δ cells, we generated line scans along hyphae and quantified their fluorescence intensity. All three organelles showed similar distribution profiles in WT and *pxdA*Δ hyphae (Figure 1, A and B, and Supplemental Figure S1), suggesting that these organelles do not use PxdA-mediated hitchhiking for transport. This data suggests that rather than being a universal hitchhiking linker, PxdA may specifically regulate peroxisome movement in *A. nidulans*.

Our finding that proper distribution of mitochondria does not require PxdA is consistent with the lack of EE-mediated hitchhiking of mitochondria observed in *U. maydis* (Guimaraes *et al.*, 2015). On the other hand, a PxdA-independent effect on the distribution of LDs was unexpected given that they hitchhike on EEs in *U. maydis*. To explore this further, we abolished EE motility by deleting the EE adaptor *hookA* (*hookA*Δ). Although peroxisome motility was severely disrupted in *hookA*Δ cells, neither the distribution nor the percentage of moving LDs was affected in *hookA*Δ or *pxdA*Δ cells compared with WT cells (Figure 1, A–D). Furthermore, though a small subset of LDs (1.85 ± 1.02% [SD]) undergo long-distance, processive movement (runs greater than 2.5 µm; Supplemental Movie S1), these runs were not colocalized with EEs (Figure 1E and Supplemental Movie S2). Consistent with the distribution data, we find no differences in the run length of LDs and only slight differences in velocity among WT, *pxdA*Δ, or *hookA*Δ strains (Supplemental Figure S2). Taken together, this data suggests that LDs do not hitchhike on EEs in *A. nidulans.*

Identification of novel *pxdA* alleles

Because our data suggest that PxdA specifically regulates peroxisome motility, we next sought to understand further the mechanisms of PxdA-mediated hitchhiking of peroxisomes. To accomplish this, we returned to candidates from a previous mutagenesis screen established to identify novel regulators required for the microtubule-based transport of peroxisomes, EEs, and/or nuclei (Tan *et al.*, 2014). In a follow-up study, we characterized two mutant strains with peroxisome-specific defects that mapped to two independent alleles in the gene *AN1156/pxdA*, which led to early stop codons

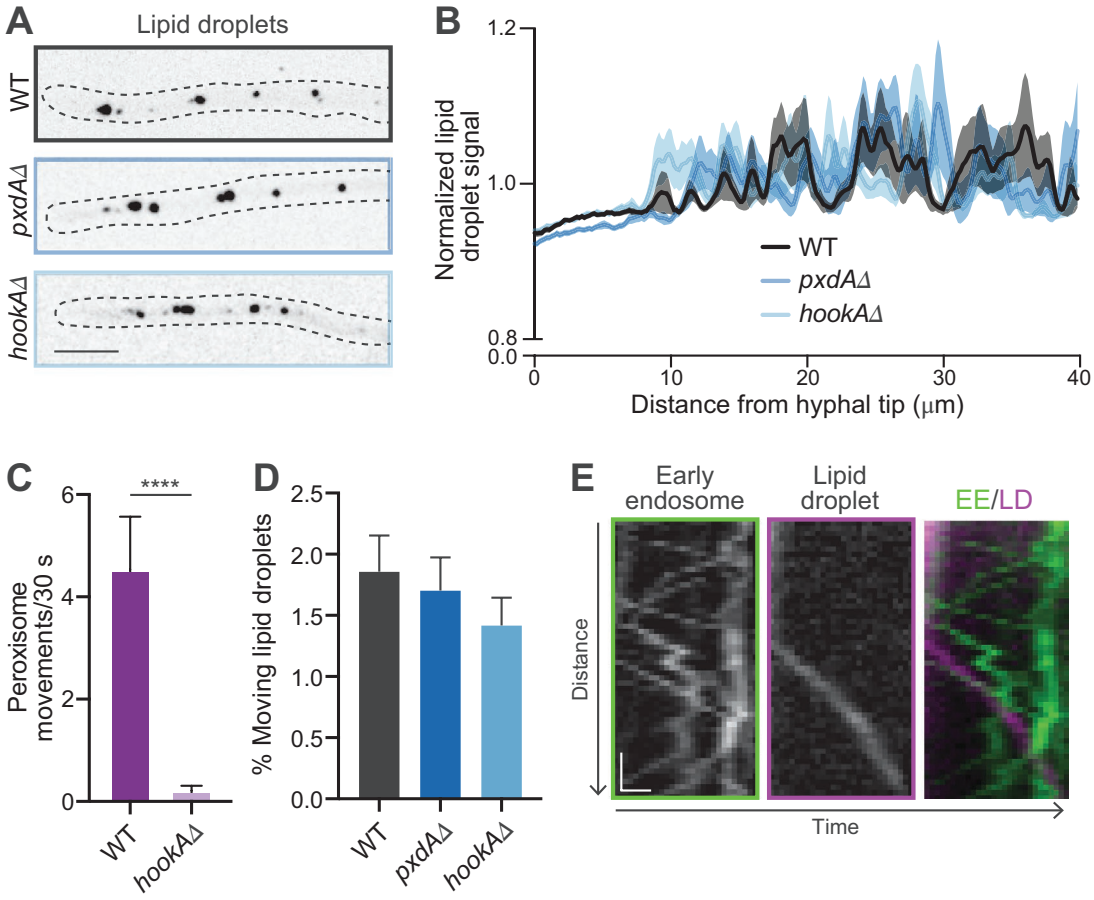

FIGURE 1: Lipid droplets (LDs) do not hitchhike on EEs in *A. nidulans*. (A) Fluorescent micrographs of LDs (Erg6/AN7146-mKate) in hyphae (outlined). Scale bar, 5 μm. (B) LD distribution is quantified by fluorescence intensity line-scans. Normalized fluorescence intensity (solid lines) ± SEM (shading) is plotted as a function of distance from the hyphal tip. n = 55 (WT), 54 (*pxdA*Δ), and 45 (*hookA*Δ) hyphae. Genotype interaction is not significant by two-way ANOVA. (C) Bar graphs of peroxisome movement in WT and *hookA*Δ hyphae, quantified as the number of peroxisomes crossing a line drawn perpendicular and 10 μm away from the hyphal tip during a 30-s time-lapse video (see *Materials and Methods*). Data is mean ± SEM. n = 13 (WT) and 19 (*hookA*Δ) hyphae. ****, $p < 0.0001$ (Mann-Whitney test). (D) Bar graphs displaying the percent motility of LDs (processive runs >2.5 μm; see *Materials and Methods*). Data is mean ± SEM. n = 14 (WT), 16 (*pxdA*Δ), and 32 (*hookA*Δ) field of views with >1000 puncta analyzed per condition. Kruskal-Wallis test was not significant. Also see Supplemental Movie S1. (E) Representative kymographs of EEs (GFP-RabA), LDs, and merged panel (EEs in green and LDs in magenta). Scale bars, 1 μm (horizontal), 2 s (vertical). Also see Supplemental Movie S2.

($PxdA_{S201stop}$ and $PxdA_{Q846stop}$) in the protein (Figure 2A; Salogiannis *et al.*, 2016). Here, we sequenced two additional mutants that showed defects in peroxisome movement and positioning. Both mutants also mapped to *pxdA*. One of the new alleles created a stop codon at Q1201 ($PxdA_{Q1201stop}$; Figure 2A), while the other allele, R2044P, was a single-residue mutation located in the coiled-coil 3 (CC3) domain of PxdA ($PxdA_{R2044P}$; Figure 2A and Supplemental Figure S3A). Both new alleles showed defects in peroxisome motility but had normal EE motility and nuclear distribution (Figure 2, B–E). We chose to focus on the $pxdA_{R2044P}$ allele as the CC3 domain of PxdA is located within a region of the protein that is necessary and sufficient for PxdA to associate with EEs (Salogiannis *et al.*, 2016).

A point mutation in PxdA decreases its ability to associate with EEs

As the R2044P mutation is present within the CC3 domain, we hypothesized that this mutation might affect the ability of PxdA to associate with EEs. To test this, we created a fluorescently tagged version of $PxdA_{R2044P}$ at the endogenous *pxdA* locus. Replacement of endogenous PxdA with $PxdA_{R2044P}$-mTagGFP2 ($PxdA_{R2044P}$-GFP) resulted in a significant decrease in peroxisome motility compared with a strain expressing WT PxdA-GFP (Figure 3A and Supplemental Movie S3). We then examined the localization and dynamics of fluorescently labeled $PxdA_{R2044P}$ compared with WT PxdA. $PxdA_{R2044P}$ showed a more diffuse localization, with few moving foci (Figure 3B and Supplemental Movie S4), suggesting a defect in $PxdA_{R2044P}$ association with EEs. Supporting this, we found that while many WT PxdA-GFP runs colocalized with EEs, there was little colocalization between $PxdA_{R2044P}$-GFP and EEs (Figure 3, C and D). A Western blot revealed that $PxdA_{R2044P}$ was expressed at similar levels as the WT protein (Supplemental Figure S3B). Thus, a single mutation in the CC3 domain of PxdA is capable of disrupting PxdA's association with EEs, resulting in decreased peroxisome hitchhiking.

PxdA interacts with the DipA phosphatase on EEs

Our screen identified four alleles of *pxdA*, but no additional genes involved in hitchhiking. To identify other proteins that might be

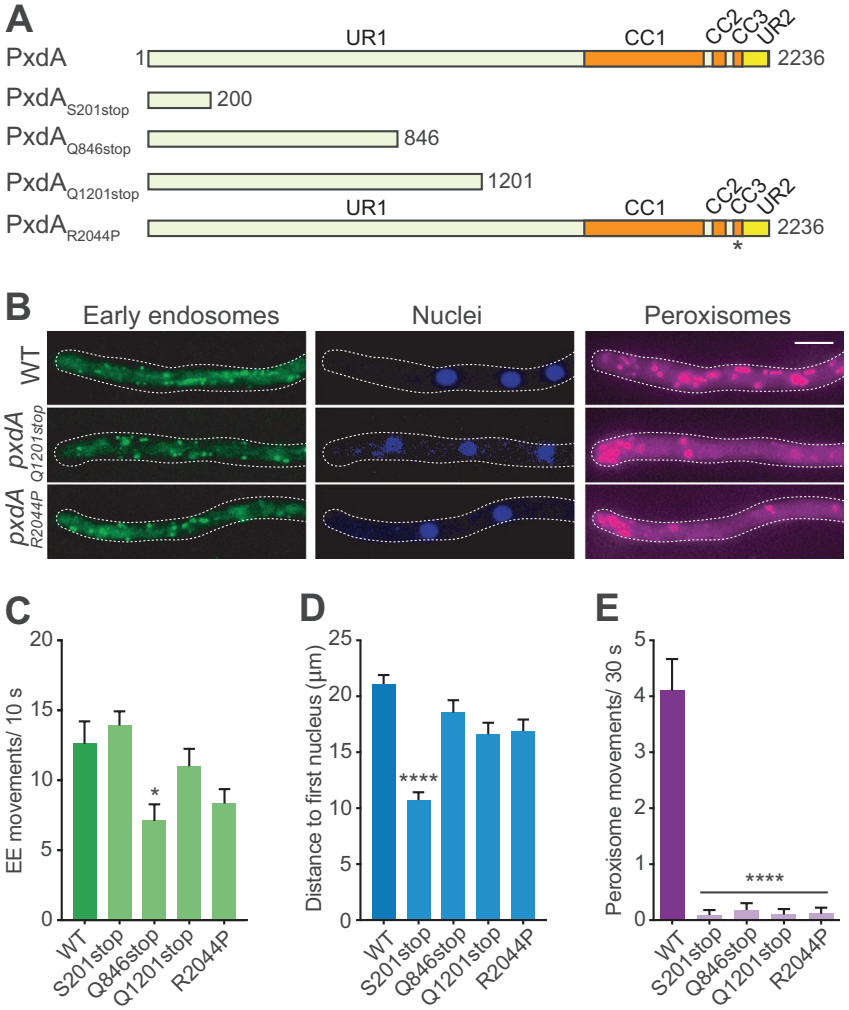

FIGURE 2: Novel *pxdA* alleles regulate peroxisome movement and distribution. (A) Schematic of PxdA domain organization and novel PxdA mutants (UR, uncharacterized region; CC, coiled coil). $PxdA_{S201stop}$, $PxdA_{Q846stop}$, and $PxdA_{Q1201stop}$ mutations create stop codons that result in truncated proteins, while the $PxdA_{R2044P}$ mutation is in the CC3 domain of PxdA (indicated by asterisk). (B) Representative images of EE (GFP-RabA), nucleus (HH1-BFP), and peroxisome (mCherry-PTS1) distribution in WT, $PxdA_{Q1201stop}$, and $PxdA_{R2044P}$ expressing hyphae. Scale bar, 5 µm. (C–E) Quantification of movement of EEs (C), distribution of nuclei (D), and movement of peroxisomes (E) in $PxdA_{Q1201stop}$ and $PxdA_{R2044P}$ compared with previously identified PxdA mutants (Salogiannis *et al.*, 2016). EE and peroxisome movement are quantified as the number of EEs or peroxisomes crossing a line drawn perpendicular and 10 µm away from the hyphal tip during a 10- or 30-s time-lapse video, respectively. Data is mean ± SEM. $n = 10$ (WT), 11 ($PxdA_{Q846stop}$), 11 ($PxdA_{S201stop}$), 10 ($PxdA_{Q1201stop}$), and 9 ($PxdA_{R2044P}$) hyphae. *, $p < 0.05$; ****, $p < 0.0001$ (Kruskal-Wallis test with Dunn's multiple comparisons test compared with WT strain).

involved in hitchhiking, we immunoprecipitated endogenously expressed PxdA followed by mass spectrometry. Specifically, we tagged PxdA at the endogenous locus with a hemagglutinin (HA) tag and performed immunoprecipitations with lysates from this strain or an untagged WT strain. PxdA resolves at approximately 250 kDa on SDS–PAGE gels when lysates are prepared under denaturing conditions (Salogiannis *et al.*, 2016). However, when lysates are prepared under nondenaturing conditions, PxdA is partially degraded (Figure 4A, and Supplemental Figure S3C). Despite this degradation, we could detect an additional faster migrating band (between 75 and 100 kDa) by Sypro stain (Figure 4A, right panel), which was present in the HA immunoprecipitations, but not the control. Mass spectrometry analysis revealed this band to be the DenA/DEN1 interacting phosphatase (DipA). DipA is a metallophosphatase that interacts with and regulates the stability of the deneddylase DenA/DEN1 on motile puncta in the cytoplasm, a process important for asexual fungal development (Schinke *et al.*, 2016).

We next sought to determine where DipA is localized, how it interacts with PxdA, and whether it regulates peroxisome movement. To accomplish this, we constructed two DipA strains: 1) an endogenously tagged DipA with two tandem copies of TagGFP2 at its carboxy terminus (DipA-GFP) to assess its localization and interaction with PxdA, and 2) a DipA deletion (*dipA*Δ) strain to assess its cellular function. As previously reported, the *dipA*Δ strain has impaired growth (Supplemental Figure S4A; Schinke *et al.*, 2016). The DipA-GFP strain grew normally (Supplemental Figure S4A), suggesting that the TagGFP2 tag does not adversely affect protein function. We performed live-cell imaging of DipA-GFP and found that it localizes to highly motile puncta, moving at ~2.5 µm per second (Figure 4B and Supplemental Movie S5), a velocity that is similar to PxdA puncta and EEs (Figure 4C; Abenza *et al.*, 2009; Egan *et al.*, 2012b; Salogiannis *et al.*, 2016). Consistent with this, the vast majority of motile DipA puncta colocalize with PxdA (Figure 4, D–F). Due to the weak fluorescence signal of DipA in our time-lapse videos, we were unable to determine the fraction of PxdA that colocalized with moving DipA foci. However, in a *hookA*Δ strain in which EEs accumulate near the hyphal tip (Zhang *et al.*, 2014), DipA displays a similar accumulation and colocalizes with PxdA (Figure 4, G and H and Supplemental Figure S4B), suggesting that DipA associates with EEs along with PxdA. To validate further the colocalization and mass spectrometry data, we performed coimmunoprecipitations with PxdA and DipA. We found that DipA-GFP was enriched in HA immunoprecipitations from PxdA-HA lysates compared with an untagged WT strain (Supplemental Figure S4C).

Because PxdA and DipA interact and colocalize on the same motile EEs, we wondered whether PxdA required DipA for its localization or vice versa. To test this, we first studied the dynamics of PxdA in the absence of DipA (*dipA*Δ). We found that PxdA displays similar localization (Figure 5A) and motility in WT versus *dipA*Δ cells (Figure 5, B and C, and Supplemental Movie S6). In contrast, DipA is largely cytosolic in *pxdA*Δ hyphae (Figure 5D) and exhibits drastically reduced long-range movement (Figure 5, E and F, and Supplemental Movie S7). There are no differences in DipA protein expression levels in *pxdA*Δ versus WT strains (Supplemental Figure S4D). These results suggest that PxdA is required for the recruitment of DipA to EEs. Consistent with this, there are fewer DipA foci and the movement of DipA is reduced in hyphae expressing the EE-binding mutant $PxdA_{R2044P}$ compared with WT hyphae (Supplemental Figure S4, E and F).

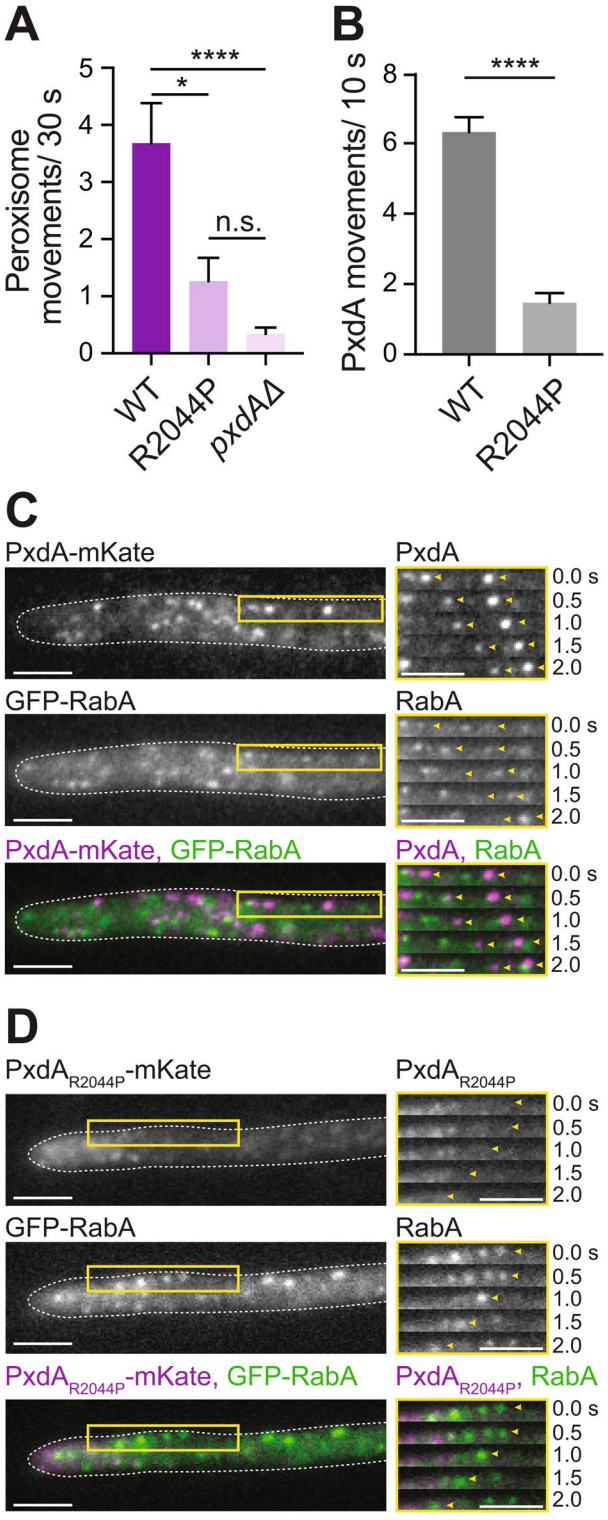

FIGURE 3: A point mutation in the CC3 domain of PxdA decreases PxdA association with EEs. (A) Bar graphs of peroxisome movements (see *Materials and Methods*) in WT, PxdA$_{R044P}$, and *pxdA*Δ hyphae. Data is mean ± SEM. n= 22 (WT), 27 (PxdA$_{R044P}$), and 38 (*pxdA*Δ) hyphae. *, p= 0.114; ****, p< 0.0001 (Kruskal-Wallis test with Dunn's multiple comparisons test). Also see Supplemental Movie S3. (B) Bar graphs of PxdA-GFP and PxdA$_{R2044P}$-GFP movements. Data is mean ± SEM. n= 17 (WT), 17 (PxdA$_{R044P}$) hyphae. ****, p< 0.0001 (Mann-Whitney test). Also see Supplemental Movie S4. (C, D) Left, representative images of hyphae expressing mTagGFP2-RabA and WT PxdA-mKate (C) or mutant PxdA$_{R044P}$-mKate (D). Scale bar, 5 μm. Right, representative time-lapse stills from the region indicated by a yellow box in the image, demonstrating colocalization of EEs (GFP-RabA) with WT PxdA (C) but not PxdA$_{R044P}$ (D). Yellow arrowheads denote processively moving EEs (GFP-RabA). Scale bar, 5 μm.

DipA regulates peroxisome movement

Based on our observations thus far, we hypothesized that DipA is required for peroxisomes to hitchhike on moving EEs. To test this, we examined peroxisome and EE distribution in a *dipA*Δ strain. Peroxisomes in *dipA*Δ hyphae displayed a slight, but significant, accumulation near the hyphal tip (Figure 6, A and B), while EEs were distributed normally (Figure 6, C and D). The *dipA*Δ strain also showed a drastic reduction in peroxisome movement, but normal movement of EEs (Figure 6, E and F, and Supplemental Movies S8 and S9). Therefore, the *dipA*Δ strain phenocopies the *pxdA*Δ strain, consistent with our observation that both proteins associate with the same subset of EEs.

Finally, we examined the localization of DipA in reference to hitchhiking peroxisomes. During peroxisome hitchhiking, PxdA-labeled EEs colocalize at the leading edge of moving peroxisomes (Guimaraes *et al.*, 2015; Salogiannis *et al.*, 2016), suggesting that PxdA and EEs might dictate the directionality of moving peroxisomes. We were curious whether moving DipA foci interacted with peroxisomes in a similar manner. We first monitored the flux of peroxisomes in the DipA-GFP strain and found that tagging DipA does not significantly perturb peroxisome movement (Supplemental Figure S4G). Next, using simultaneous two-color imaging of DipA and peroxisomes, we found that motile DipA localizes to the leading edge of peroxisomes (Figure 6, G and H), similar to PxdA (Salogiannis *et al.*, 2016). In further support of this, DipA shifts to the leading edge of peroxisomes concurrent with rapid directional switches in peroxisome movement (Figure 6G and Supplemental Movie S10). In summary, we find that DipA localizes to PxdA-labeled EEs and is critical for peroxisome hitchhiking.

DISCUSSION

Proper cargo transport is critical for many cell types, including filamentous fungi, in which cellular cargoes are evenly distributed along their hyphae. Hitchhiking is a mode of transport whereby one type of cargo achieves motility via attachment to another type of motile cargo. We previously found that the protein PxdA is required for peroxisomes to hitchhike on EEs in *A. nidulans*. In this study, we find that PxdA specifically regulates peroxisomes, whereas LD, mitochondria, and preautophagosome distribution are not affected in the absence of PxdA. We identified two novel mutant alleles of PxdA, including a single-residue mutation (PxdA$_{R2044P}$) that disrupts PxdA association with EEs. We also identified a novel regulator of peroxisome hitchhiking, the phosphatase DipA. DipA is required for peroxisome motility, colocalizes with PxdA, and its association with EEs requires PxdA. Together, these data provide further insight into factors that affect peroxisome hitchhiking in *A. nidulans*.

LDs do not hitchhike on EEs in *Aspergillus*

Unlike *U. maydis*, LDs do not hitchhike on EEs in *A. nidulans*. We conclude this for the following reasons: First, the movement and distribution of LDs is similar to WT in both *pxdA*Δ and *hookA*Δ strains (Figure 1, A, B, and D, and Supplemental Figure S2A), the latter of which completely abolishes EE motility. Second, we did not detect any cotransport between EEs and LDs (Figure 1E). Third, the velocity of LDs in *A. nidulans* is less than 1 μm/s (Supplemental

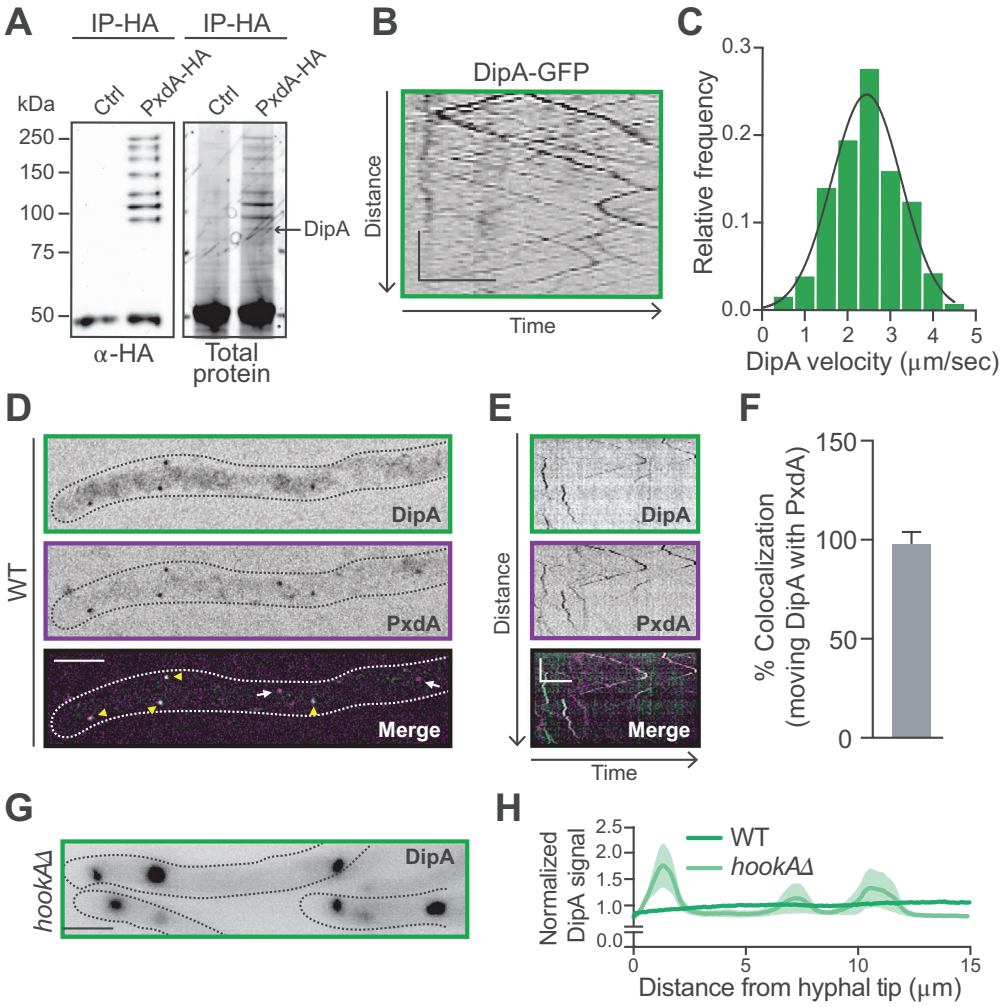

FIGURE 4: DipA associates with PxdA-marked endosomes. (A) Anti-HA Western blot (left) and Sypro Ruby–stained SDS–PAGE gel (right) of lysates incubated with HA-conjugated agarose from WT or PxdA-HA expressing hyphae. Mass spectrometry identified DipA (indicated by arrow) from two biological replicates. (B) Representative kymograph of DipA-GFP movement. Scale bars, 5 μm (horizontal), 5 s (vertical). Also see Supplemental Movie S5. (C) Histogram of DipA-GFP velocities calculated from kymographs as in B. Mean velocity is 2.44 ± 0.77 (SD) μm/s. $n = 257$ moving events. (D) Colocalization of DipA-GFP and PxdA-mKate along a hypha. Scale bar, 5 μm. (E) Representative kymograph of DipA and PxdA comovement in a WT hyphae. Scale bar, 5 μm (horizontal), 10 s (vertical). (F) Quantification of the percent overlap of DipA colocalized with PxdA. Mean percent overlap is 97.88 ± 6.01 (SD). $n = 8$ kymographs. (G) Representative image of DipA-GFP distribution in *hookA*Δ hyphae. Scale bar, 5 μm. (H) DipA-GFP distribution is quantified by fluorescence intensity line-scans of fluorescently tagged organelles in WT or *hookA*Δ hyphae. Mean fluorescence intensity (solid lines) ± SEM (shading) is plotted as a function of distance from the hyphal tip. $n = 3$ (WT) and 7 (*hookA*Δ) hyphae.

Figure S2B), which is much slower than the velocity of EEs, PxdA, and DipA foci (~2.5 μm/s).

These findings suggest that *U. maydis* and *A. nidulans* potentially have very different modes of organelle distribution and transport. Indeed, the *A. nidulans* peroxisome hitchhiking tether PxdA is not conserved in *U. maydis*, and the regions of the *U. maydis* ribonucleoprotein tether Rrm4/Upa1 required for hitchhiking are not conserved in *A. nidulans* (Pohlmann *et al.*, 2015), suggesting that distinct hitchhiking machineries have evolved in *U. maydis* and *A. nidulans*. Furthermore, while multiple cargoes have been demonstrated to hitchhike in *U. maydis* (Salogiannis and Reck-Peterson, 2017), thus far we have identified peroxisomes as the only hitchhiking cargo in *A. nidulans*. Peroxisomes in *A. nidulans* can mature into Woronin bodies, organelles crucial for septal pore blocking in *A. nidulans* and other filamentous Ascomycota species (Markham and Collinge, 1987; Jedd and Chua, 2000; Steinberg *et al.*, 2017). One possibility is that peroxisome-specific hitchhiking promotes the even distribution of peroxisomes along the hyphae, allowing proper septal pore blocking. Future work will be needed to identify how the transport and distribution of LDs and other cargoes are regulated in different filamentous fungi.

A single-residue mutation in PxdA disrupts its association with EEs

We previously showed that the CC2 and CC3 domains of PxdA are required for its association with EEs (Salogiannis *et al.*, 2016). Here, we found that a PxdA mutant allele (*pxdA*$_{R2044P}$) disrupts PxdA association with EEs via a single amino acid change in coiled-coil

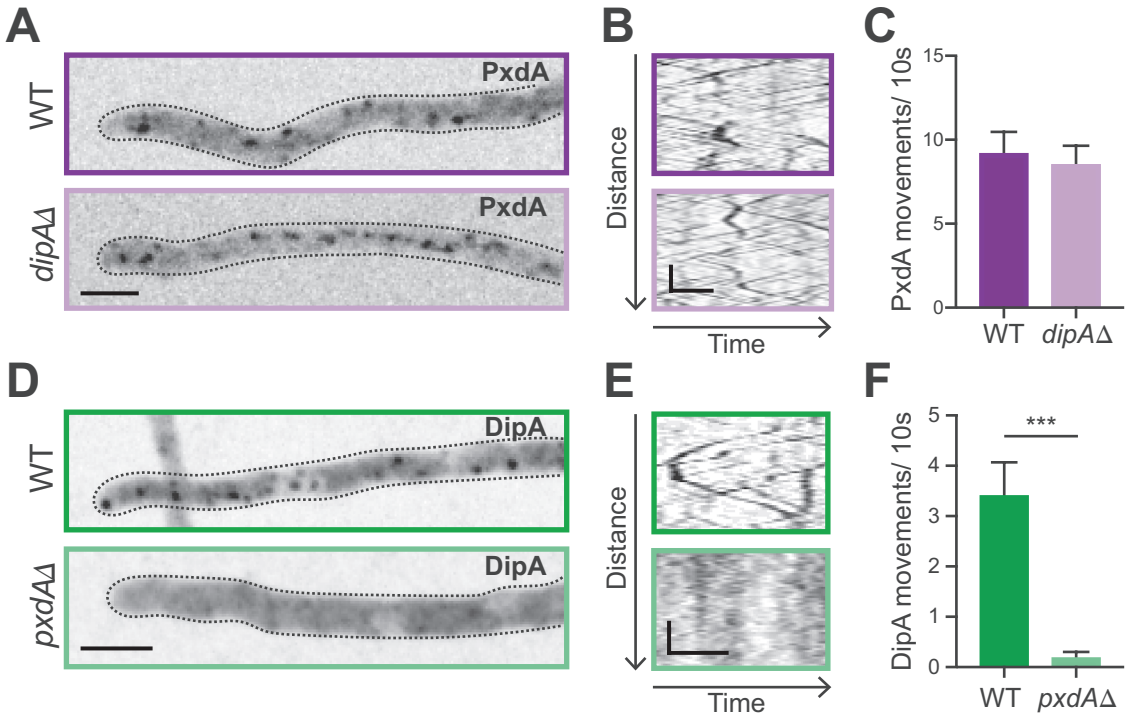

FIGURE 5: PxdA is required for DipA localization on moving foci. (A) Representative micrograph of GFP-PxdA puncta along a WT or *dipA*Δ hypha. Scale bar, 5 µm. (B) Representative kymograph of PxdA movement in a WT (top) or *dipA*Δ (bottom) background. Scale bars, 2.5 µm (horizontal), 5 s (vertical). Also see Supplemental Movie S6. (C) Bar graph of the flux of PxdA movements in WT and *dipA*Δ hyphae calculated as the number of PxdA foci crossing a line drawn perpendicular and 10 µm away. $n = 6$ (WT) and 10 (*dipA*Δ) hyphae. (D) Representative micrograph of DipA-GFP puncta along a WT or *pxdA*Δ hypha. Scale bar, 5 µm. (E) Representative kymograph of DipA movement in a WT (top) or *pxdA*Δ (bottom) background. Scale bars, 2.5 µm (horizontal), 5 s (vertical). Also see Supplemental Movie S7. (F) Bar graph of DipA movements in WT and *pxdA*Δ hyphae. $n = 25$ (WT) and 11 (*pxdA*Δ) hyphae. ***, $p = 0.0002$ (Mann-Whitney test).

region CC3 (Figure 2A and Figure 3, C and D). This mutation may disrupt PxdA's ability to interact with a binding partner on the EE surface or with the EE membrane directly. The $PxdA_{R2044P}$ mutant will be an important tool in the future to characterize how PxdA associates with EEs and whether PxdA directly or indirectly links EEs to hitchhiking cargoes.

DipA is a regulator of peroxisome hitchhiking

Our mass spectrometry experiment identified the phosphatase DipA as a PxdA interactor (Figure 4A). DipA associates with the PxdA-bound population of EEs (Figure 4, D–F) and is required for peroxisomes to hitchhike on EEs (Figure 6, E, G, and H). Additionally, DipA requires PxdA to associate with EEs (Figure 5, D–F, and Supplemental Figure S4, E and F). DipA is a phosphatase whose function was previously linked to regulating the phosphorylation status and degradation of DenA/Den1, a protein involved in asexual spore formation (Christmann *et al.*, 2013; Schinke *et al.*, 2016). DenA is cotransported with DipA (Schinke *et al.*, 2016). Given the similar cotransport of both DenA and PxdA with DipA, it is possible that DipA also regulates PxdA by modulating PxdA's phosphorylation state. Future work will determine whether PxdA is phosphorylated, whether its phosphorylation state is regulated by DipA, and whether DenA is required for hitchhiking.

Though we do not understand how the PxdA-DipA complex links to peroxisomes, it is also possible that DipA regulates the phosphorylation state of other proteins in the hitchhiking machinery, such as peroxisome-associated proteins. Alternatively, DipA may not regulate the phosphorylation state of the hitchhiking machinery at all but may instead link PxdA to peroxisomes. Whether DipA links PxdA to peroxisomes or whether DipA regulates hitchhiking in other ways remains to be determined.

MATERIALS AND METHODS

Fungal growth conditions

A. nidulans strains were grown in yeast extract and glucose (YG) medium or 1% glucose minimal medium (Nayak *et al.*, 2006), supplemented with 1 mg/ml uracil, 2.4 mg/ml uridine, 2.5 µg/ml riboflavin, 1 µg/ml para-aminobenzoic acid, and 0.5 µg/ml pyridoxine when required. Glufosinate (Sigma) for *bar* selection was used at a final concentration of 700 µg/ml (Straubinger *et al.*, 1992).

For imaging of germlings, spores were resuspended in 0.5 ml 0.01% Tween-80 solution. The spore suspension was diluted at 1:1000 in liquid minimal medium containing appropriate auxotrophic supplements. The spore and media mix (400 µl) was added to an eight-chambered Nunc Lab-Tek II coverglass (ThermoFisher) and incubated at 30°C for 16–20 h before imaging. For imaging of mature hyphae, spores were inoculated on minimal medium plates containing the appropriate auxotrophic supplements and incubated at 37°C for 12–16 h. Colonies were excised from agar plates and inverted on Lab-Tek plates for imaging. For biochemistry, spores were inoculated in YG medium containing the appropriate auxotrophic supplements for 16–20 h at 37°C either shaking at 200 rpm in an Erlenmeyer flask or incubated in 100-mm Petri dishes.

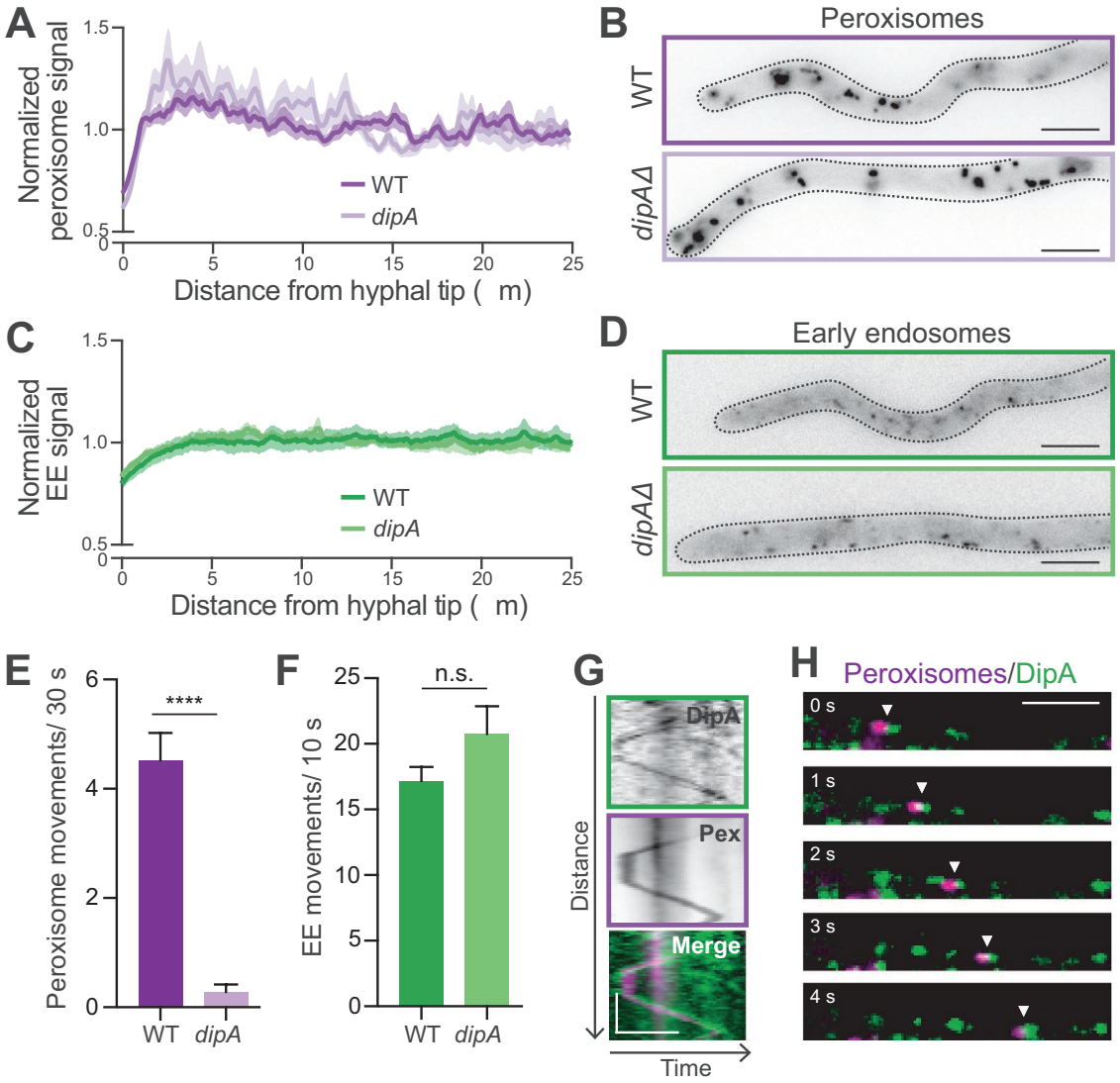

FIGURE 6: DipA regulates the movement and distribution of peroxisomes. (A) Distribution of peroxisomes along WT and *dipA*Δ hyphae. Data is normalized mean intensity ± SEM. $n = 22$ (WT) and 20 (*dipA*Δ) hyphae. Distribution comparing genotypes is significant ($p < 0.0001$) by two-way ANOVA. (B) Representative micrographs of peroxisomes along WT and *dipA*Δ hyphae. Scale bar, 5 µm. (C) Distribution of EEs along WT and *dipA*Δ hyphae. $n = 7$ (WT) and 6 (*dipA*Δ) hyphae. Distribution comparing genotypes is not significant by two-way ANOVA. (D) Representative micrographs of EEs along WT and *dipA*Δ hyphae. Scale bars, 5 µm. (E) Bar graph of the flux of peroxisome movements in WT and *dipA*Δ hyphae calculated as the number of peroxisomes crossing a line drawn perpendicular and 10 µm away from (*dipA*Δ) hyphae. ****, $p < 0.0001$, Mann-Whitney test. Also see Supplemental Movie S8. (F) Bar graph displaying movements of EEs in WT and *dipA*Δ hyphae. $n = 7$ (WT) and 16 (*dipA*Δ) hyphae. Also see Supplemental Movie S9. (G, H) Kymographs (G) and time-lapse stills (H) of DipA-GFP with moving peroxisomes. Scale bars, 5 µm (horizontal) and 5 s (vertical). Also see Supplemental Movie S10.

Plasmid and strain construction

Strains of *A. nidulans* used in this study are listed in Supplemental Table S1. All strains were confirmed by a combination of PCR and/or sequencing from genomic DNA isolated as previously described (Lee and Taylor, 1990) and in some cases by Western blot analysis. For all plasmids, PCR fragments were inserted into the Blue Heron Biotechnology pUC vector at 5′*Eco*RI and 3′*Hind*III restriction sites using Gibson isothermal assembly (Gibson *et al.*, 2009). All plasmids were confirmed by Sanger sequencing. Initial strains were created by homologous recombination with linearized DNA to replace the endogenous gene in strains lacking *ku70* with *Afribo* (*Aspergillus fumigatus Ribo*), *AfpyrG* (*Aspergillus fumigatus pyrG*), or *Afpyro* (*Aspergillus fumigatus pyro*), or *bar* as selectable markers (Straubinger *et al.*, 1992; Nayak *et al.*, 2006). Additional strains were created using genetic crossing as previously described (Todd *et al.*, 2007). The strategies for transforming *hookA*Δ, *pxdA*Δ, PxdA-HA, PxdA-mTagGFP2, and PxdA-mKate2 strains, as well as the strains containing fluorescently labeled EEs, peroxisomes, and nuclei, have been previously described (Tan *et al.*, 2014; Salogiannis *et al.*, 2016). The strategies for DNA constructs and strains created for the current study are as follows.

PxdA$_{R2044P}$-GFP/mKate. To construct this plasmid, carboxy-terminal codon-optimized fluorescent protein tags, either mTagGFP2

(Subach *et al.*, 2008) or mKate2 (Shcherbo *et al.*, 2009), were preceded by a GA(x4) linker and followed by *AN1156/pxdA*'s native 3′ UTR with flanking 1 kb upstream and downstream homologous recombination arms. To introduce the R2044P mutation, the upstream 1 kb recombination arm was amplified by PCR from genomic DNA (gDNA) isolated from RPA568 (mutagenized strain harboring the R2044P mutation) using the oligos 5′-GTCACGACGTTGTAAAACGACGGCCAGTGCCTTCAGGAGCGAGTGGCGCATCCGAAG-3′ and 5′-CTGACATTGCACCTGCACCTGCACCTGCACCTGCTATTTGTGG GCCAAAGGGACCGTCGG-3′. To amplify the linearized DNA used for targeting via transformation, the oligos 5′-CCTTCAGGAGCGAGTGGCGCATCTC-3′ and 5′-GACGTTGACACTTCGTGCTAGAACT-3′ were used.

GFP-PxdA. This N-terminal GFP-tagged PxdA construct was used for data collected in Figure 5, A–C. For ease of cloning, this construct lacks the first 816 aa of PxdA (PxdA$\Delta_{1\text{-}816}$ starts with 5′-CAGCAGGTCCCGGTTCCAC-3′ for reference), but is functional because it has no effect on peroxisome motility and distribution (unpublished data; Salogiannis *et al.*, 2016). Codon-optimized mTagGFP2 with a GA(x4) linker was followed by the PxdA$(\Delta_{1\text{-}816})$ fragment (4260 base pairs), its native 3′ UTR and an *AfpyrG* cassette, and flanked by 1 kb homologous recombination arms. To amplify the linearized DNA used for transformations, the oligos 5′-AGTCGACACGGAAGGTTGGTCAATC-3′ and 5′-GACGTTGACACTTCGTGCTAGAACT-3′ were used. To identify positive clones with better efficiency, we targeted the linear PxdA$(\Delta_{1\text{-}816})$-*AfpyrG*–containing DNA into a *pxdA*Δ strain (RPA921) where the endogenous *pxdA* locus was replaced with *Afribo*. Using this strategy, we positively selected clones that 1) grow on minimal media plates lacking supplemented uradine–uracil and 2) are unable to grow on plates lacking riboflavin. From there, we sequence-verified this strain and used genetic crosses to generate additional strains.

***dipA*Δ.** This strain was previously published elsewhere (Schinke *et al.*, 2016), but was remade for this study using a different strategy. Linearized DNA used for targeting was amplified with 5′-ATGAGACGAACCTGGCCATCAAGGC-3′ and 5′-TTATGCCATGTTGCAGGTGGAA CA-3′ by fusion PCR (Szewczyk *et al.*, 2006) with fragments for a selectable marker flanked by upstream and downstream homologous recombination arms around the *AN10946/dipA* genomic locus.

DipA-GFP. A tandem 2x-mTagGFP2 preceded by a GA(x4) linker and followed by *AN10946/dipA*'s native 3′ UTR with flanking 1 kb upstream and downstream homologous recombination arms. This plasmid was digested with the *Pci*I restriction enzyme (cut sites in the 5′ and 3′ homologous arms) to linearize DNA for targeting.

AN7146-mKate (LDs). To visualize endogenously labeled LDs, we fluorescently tagged AN7146 (a putative S-adenosyl-methionine delta-24-sterol-C-methyltransferase). AN7146 is a homologue of Erg6 in *U. maydis* and used as a LD marker in a previous study (Guimaraes *et al.*, 2015). To create this plasmid, C-terminal codon-optimized mKate2 was preceded by a GA(x4) linker and followed by *AN7146*'s native 3′ UTR with flanking 1 kb upstream and downstream homologous recombination arms. The oligos 5′-GTTGTTCAAAACCCTTGGGAAATTTG-3′ and 5′-TCCAGTTGAAGTACACTACACATTCG-3′ were used to amplify the linearized DNA fragment used for targeting.

GFP-AtgH (preautophagosomes). To visualize preautophagosome puncta, we fluorescently tagged the functional homologue of Atg8, *atgH/AN5131* (Pinar *et al.*, 2013). To construct this plasmid, the codon-optimized mTagGFP2 followed by a GA5 linker and the entire *atgH* locus (including its native 3′ UTR) was flanked by homologous recombination arms. The oligos 5′-CTGTAAATTCTTTCTTGCCC-3′ and 5′-CTTTGCCGTCGTATCGACC-3′ were used to PCR amplify the targeting construct used for transformation. All experiments using this strain were cultured in standard media (not under starvation conditions).

Tom20-GFP (mitochondria). To visualize mitochondria, we fluorescently tagged the mitochondrial outer membrane component *AN0559*/Tom20 (Suresh *et al.*, 2017). To construct this plasmid, a codon-optimized 2x-mTagGFP2 was preceded by a GSGSG linker and followed by *AN0559*'s native 3′ UTR with flanking 1 kb upstream and downstream homologous recombination arms. The oligos 5′-GGGCGGCGATTTTTGCTGCGAAGAG-3′ and 5′-CGGATTTGCCGTCAACGGCGTTGGT-3′ were used to amplify the linearized DNA fragment used for targeting.

Whole-genome sequencing

The general workflow for whole-genome sequencing has been previously described (Tan *et al.*, 2014). The mutagenized strains, RPA568 and RPA639, were backcrossed to the parental RPA520 strain while tracking the presence of the peroxisome accumulation and motility phenotypes in order to 1) reduce the number of background mutations and 2) to ensure the phenotype likely arose from a single gene (similar to Tan *et al.*, 2014). gDNA was prepared from a pool of at least five individual backcrossed strains and treated with RNase before a final cleanup by phenol/chloroform extraction. gDNA was sheared with the Covaris S2 sonicator, and samples were run on a D1000 Tapestation to evaluate shearing success. Samples were normalized to the same input and prepped using KAPA HTP Library Prep Reagents using an Apollo 324 robot. This involved end-repair, A-tailing, and adapter ligation, followed by amplification and barcoding (similar to [Tan *et al.*, 2014]). A bead-based cleanup removed primer dimers and adapter dimers. The final library products were run on a High Sensitivity D1000 Screentape and qPCR was performed using the KAPA Library Quantification kit. The libraries were then pooled and loaded onto an individual lane of the HiSeq 2500 Rapid flowcell, with a read length of ~50 base pairs. Data sets were sorted by barcode using Python software as previously described and the data were aligned using the *A. nidulans* reference genome FGSC_A4 (*Aspergillus* genome database; AspGD; aspgd.org). Genomic data was sorted for genomic feature (i.e., exon, intron) and mined specifically at the *AN1156/pxdA* locus for high quality (more than five times in the mutant data set and zero in the backcrossed WT mutagenized strain) and uncommon (i.e., not in the WT backcrossed strain) nonsynonymous mutations.

Imaging acquisition

All images were collected at room temperature. Imaging experiments in Figure 2, Figure 3, Figure 4, B, C, G, and H, Figure 6, A–F, Supplemental Figure S1, and Supplemental Movies S2–S4, S6, and S8–S10 were acquired using an inverted microscope (Nikon, Ti-E Eclipse) equipped with a 60× and 100× 1.49 NA oil immersion objective (Nikon, Plano Apo), and a MLC400B laser launch (Agilent), with 405 nm, 488 nm, 561 nm, and 640 nm laser lines. Excitation and emission paths were filtered using single bandpass filter cubes (Chroma). For two-color colocalization imaging in Figure 2, the emission signals were further filtered and split using W-view Gemini image splitting optics (Hamamatsu). Emitted signals were detected with an electron multiplying CCD camera (Andor Technology, iXon

Ultra 888). Illumination and image acquisition were controlled with NIS Elements Advanced Research software (Nikon), and the xy position of the stage was controlled with a ProScan linear motor stage controller (Prior). Simultaneous two-color time-lapse images in Figure 4, D–F, and Figure 6, G and H were collected using a Plan Apo TIRF 60×/1.49 oil immersion objective on the Deltavision OMX Blaze V4 system (GE Healthcare). GFP and mKate2/mCherry were excited simultaneously with 488 nm and 568 nm diode laser lines, respectively. A BGR polychroic mirror was used to split emission light from fluorophores to different PCO Edge sCMOS cameras. Emission filters in front of both cameras were used to select appropriate wavelengths (528/48 nm and 609/37 nm for GFP and mKate/mCherry, respectively). Images were aligned with OMX image registration using softWoRx software and some images were deconvolved for display using the enhanced ratio method.

For imaging experiments in Figure 1, A–D, Supplemental Figure S2, Figure 5, and Supplemental Movies S1, S5, and S7, spinning-disk confocal microscopy was performed using a Yokogawa W1 confocal scanhead mounted to a Nikon Ti2 microscope with an Apo TIRF 100× 1.49 NA objective. The scope was controlled via NIS Elements using the 488 nm and 561 nm lines of a six-line (405 nm, 445 nm, 488 nm, 515 nm, 561 nm, and 640 nm) LUN-F-XL laser engine and a Prime95B camera (Photometrics). Image channels were acquired using bandpass filters for each channel (525/50 nm and 595/50 nm). Z-stacks were acquired using a piezo Z stage (Mad City Labs).

Image and data analysis

Line-scan distribution and flux measurements were calculated as previously reported (Salogiannis *et al.*, 2016). For line-scan measurements, maximum-intensity projections of fluorescence micrographs and brightfield images (for hyphae) were obtained using ImageJ/FIJI (National Institutes of Health, Bethesda, MD). Brightfield images were traced starting from the hyphal tip, using the segmented line tool (line width 25), and traces were superimposed on the fluorescence micrographs to project the average fluorescence intensity. For normalization of line-scans, each condition's average immunofluorescence intensity values at each point along the hyphae were normalized against that condition's total baseline average. For organelle flux measurements, the number of puncta crossing a line approximately 10 µm perpendicular to and from the hyphal tip was manually counted. All peroxisome movement data were calculated from 30 s time-lapse videos, while all EE, DipA, and PxdA flux data were calculated from 10 s time-lapse videos. DipA velocity (Figure 4C) and lipid droplet velocity (Supplemental Figure S2B) were analyzed using ImageJ. Specifically, maximum-intensity projections were generated from time-lapse sequences to define the trajectory of particles of interest. The segmented line tool was used to trace the trajectories and map them onto the original video sequence, which was subsequently resliced to generate a kymograph. The instantaneous velocities and run lengths of individual particles were calculated from the inverse of the slopes of kymograph traces. To calculate the percent motility of LDs (Figure 1), 3 min time-lapse movies of a field of view of mature hyphae (containing segments of ~5–15 cells) expressing fluorescently labeled LDs (AN7146-mKate) were imaged at 500-ms intervals. After background subtraction in ImageJ, moving LDs were initially assessed visually and kymographs were subsequently generated (as described above) from these moving puncta. Each LD puncta was scored as moving if it exhibited a directed run (no pauses) greater than 2.5 µm during its movement. This number was divided by the total number of LD puncta in the field of view, which was calculated by using the "find maxima" tool in ImageJ on the first frame of each movie. At least 50 LDs were analyzed per field of view and more than 1000 total LDs were analyzed per condition across three separate days. For distance to first nucleus measurements (Figure 2D), nuclei were thresholded in ImageJ and the segmented line tool was used to measure the distance from the hyphal tip to the edge of the first nucleus.

For DipA/PxdA colocalization measurements, DipA and PxdA kymographs were generated from simultaneous two-color time-lapse videos. DipA kymographs were thresholded in ImageJ, manually traced using the segmented line tools, and traces were then superimposed onto the PxdA kymograph to manually determine overlap. The fractional overlap (colocalization) of DipA with PxdA for each kymograph was calculated.

All statistical analyses were performed using Prism8 (GraphPad).

Cell lysis and immunoprecipitations

Overnight cultures for biochemistry were strained in miracloth (Millipore), flash-frozen in liquid nitrogen, and ground with a mortar/pestle in the presence of liquid nitrogen. For Western blot analysis of DipA-GFP in WT and *pxdA*Δ strains (Supplemental Figure S4C), PxdA-GFP and $PxdA_{R2044P}$-GFP comparisons (Supplemental Figure S3B), and Western blot analysis of PxdA-TurboID-3xFLAG strain in urea buffer (Supplemental Figure S3C), 250 µl of packed ground mycelia were resuspended in 500 µl boiling denaturing buffer (125 mM Tris-HCl, pH 7.0, 8 M urea, 1 mM EDTA, pH 7.0, 2% SDS, 10 mM dithiothreitol (DTT), 10% beta-ME, 4% glycerol), rotated for 10 min at room temperature (RT), spun at 20,000 ×*g* for 10 min at RT, and followed by the addition of 1x Laemmli buffer (BioRad) to the supernatant. For Western blot analysis of PxdA-TurboID-3xFLAG strain in RIPA buffer (Supplemental Figure S3C), 250 µl of packed ground mycelia were resuspended in 500 µl of RIPA buffer (50 mM Tris-HCl, pH 8.0, 150 mM NaCl, 1% [vol/vol] NP-40, 0.5% [wt/vol] sodium deoxycholate, 0.1% [wt/vol] SDS, 1 mM DTT) with added protease inhibitors (cOmplete Protease Inhibitor Cocktail; Roche, Switzerland) at 4°C rotated for 10 min at RT, spun at 20,000 ×*g* for 10 min at RT, and followed by the addition of 1x Laemmli buffer (BioRad) to the supernatant. For anti-HA immunoprecipitations from WT and PxdA-HA strains used for mass spectrometry analysis (Figure 4A), all steps were performed at 4°C unless otherwise stated. Approximately 4 ml packed ground mycelia were lysed in 10 ml IP lysis buffer (150 mM NaCl, 50 mM Tris, pH 8.0, 1% Triton X-100, 0.1% SDS) supplemented with protease inhibitor cocktail (Roche). Lysates were rotated for 30 min at 4°C and centrifuged for 5 min at 1000 ×*g*. Supernatants were subjected to two additional 20,000 × *g* spins for 20 min each. Agarose beads were added to clarified supernatants and rotated end-over-end for 1 h to preclear any nonspecific interactions. Precleared lysate was incubated with HA-conjugated agarose beads (ThermoFisher) and rotated over-end for 1.5 h. Beads were washed 3x with cold modified RIPA buffer and were subsequently boiled in Laemmli buffer for 5 min prior to running on an SDS–PAGE gel. For coimmunoprecipitation between PxdA and DipA (Supplemental Figure S4C), 1 ml packed mycelia were lysed in 2.5 ml of IP lysis buffer (150 mM NaCl, 50 mM Tris pH 8.0, 1% Triton X-100) without SDS, rotated at 4°C, and subjected to a 20,000 × *g* spins for 20 min. Supernatants were incubated with 50 µl HA-conjugated agarose beads and rotated end-over-end for 1.5 h at 4°C. Beads were washed three times with cold buffer and were subsequently boiled in Laemmli buffer for 5 min before running on an SDS–PAGE gel.

Western blotting and mass spectrometry

All protein samples were resolved on 4–12% gradient SDS–PAGE gels (Life Technologies) for 60 min at 150 V. For Western blotting,

gels were transferred to nitrocellulose for 3 h at 250 mA in 4°C. Blots were blocked with 5% milk in TBS-0.1% Tween-20 (TBS-T). Antibodies were diluted in 5% milk in TBS-T. Primary antibodies were incubated overnight at 4°C and horseradish peroxidase (HRP)–conjugated secondary antibodies (ThermoFisher) were incubated at RT for 1 h. Rabbit anti-Tag(CGY)FP (Evrogen) was used at 1:1000 to detect mTagGFP2. Mouse anti-HA (Sigma) was used at 1:1000. Secondary antibodies were used at 1:10,000. Blots were rinsed three times with TBS-T for 10 min after primary and secondary antibodies. Electrochemiluminescence was produced with HRP and Prosignal Pico (Prometheus) detection reagent and imaged on a ChemiDoc (BioRad) using Image Lab (v5.2.1.) software.

For Sypro protein staining and subsequent mass spectrometry of anti-HA immunoprecipitations (Figure 4A), SDS–PAGE gel was incubated in Sypro Red protein gel stain (ThermoFisher) at 1:5000 in 7.5% acetic acid for 45 min. The band of interest was excised and submitted to the Taplin Mass Spectrometry Facility at Harvard Medical School. A before and after picture using Sypro Ruby detection on the ChemiDoc (BioRad) was obtained to ensure the correct bands were excised. Excised gel bands were cut into approximately 1 mm^3 pieces. Gel pieces were then subjected to a modified in-gel trypsin digestion procedure (Shevchenko *et al.*, 1996). Gel pieces were washed and dehydrated with acetonitrile for 10 min followed by removal of acetonitrile. Pieces were then completely dried in a speed-vac. Rehydration of the gel pieces was with 50 mM ammonium bicarbonate solution containing 12.5 ng/µl modified sequencing-grade trypsin (Promega; Madison, WI) at 4°C. After 45 min, the excess trypsin solution was removed and replaced with 50 mM ammonium bicarbonate solution to just cover the gel pieces. Samples were then placed in a 37°C room overnight. Peptides were later extracted by removing the ammonium bicarbonate solution, followed by one wash with a solution containing 50% acetonitrile and 1% formic acid. The extracts were then dried in a speed-vac (~1 h) and stored at 4°C until analysis. On the day of analysis, the samples were reconstituted in 5–10 µl of HPLC solvent A (2.5% acetonitrile, 0.1% formic acid). A nanoscale reverse-phase HPLC capillary column was created by packing 2.6 µm C18 spherical silica beads into a fused silica capillary (100 µm inner diameter ×~30 cm length) with a flame-drawn tip. After equilibrating the column each sample was loaded via a Famos auto sampler (LC Packings, San Francisco, CA) onto the column. A gradient was formed and peptides were eluted with increasing concentrations of solvent B (97.5% acetonitrile, 0.1% formic acid). As peptides eluted, they were subjected to electrospray ionization and then entered into an LTQ Orbitrap Velos Pro ion-trap mass spectrometer (Thermo Fisher Scientific, Waltham, MA). Peptides were detected, isolated, and fragmented to produce a tandem mass spectrum of specific fragment ions for each peptide. Peptide sequences (and hence protein identity) were determined by matching to the *A. nidulans* FGSC A4 protein database in Uniprot (https://www.uniprot.org/proteomes/UP000000560) with the acquired fragmentation pattern by the software program, Sequest (Thermo Fisher Scientific). All databases include a reversed version of all the sequences and the data was filtered to between a 1 and 2% percent peptide false discovery rate.

ACKNOWLEDGMENTS

We thank Stephen A. Osmani for personal communication and sharing unpublished data on DipA and Thomas L. Schwarz for his guidance and supervision of J.S. for part of this project. We also thank the Nikon Imaging Centers at Harvard Medical School and University of California, San Diego for technical support and advice, Ross Tomaino and the Taplin Mass Spectrometry Facility at Harvard Medical School for technical support on mass spectrometry experiments, and the Bioinformatics Department at the Harvard T.H. Chan School of Public Health for assisting with whole-genome sequencing data analysis. J.S. was funded for part of this work by the Charles King Trust Fellowship supported by the Charles H. Hood Foundation (Boston, MA). J.R.C. was funded by a postdoctoral fellowship from the National Institutes of Health (Grant no. F32GM-126692). S.L.R.-P. is an investigator of the Howard Hughes Medical institute and is also supported by Grant no. R01GM-121772.

REFERENCES

Abenza JF, Pantazopoulou A, Rodríguez JM, Galindo A, Peñalva MA (2009). Long-distance movement of *Aspergillus nidulans* early endosomes on microtubule tracks. Traffic 10, 57–75.

Baumann S, König J, Koepke J, Feldbrügge M (2014). Endosomal transport of septin mRNA and protein indicates local translation on endosomes and is required for correct septin filamentation. EMBO Rep 15, 94–102.

Baumann S, Pohlmann T, Jungbluth M, Brachmann A, Feldbrügge M (2012). Kinesin-3 and dynein mediate microtubule-dependent co-transport of mRNPs and endosomes. J Cell Sci 125, 2740–2752.

Bielska E, Schuster M, Roger Y, Berepiki A, Soanes DM, Talbot NJ, Steinberg G (2014). Hook is an adapter that coordinates kinesin-3 and dynein cargo attachment on early endosomes. J Cell Biol 204, 989–1007.

Christmann M, Schmaler T, Gordon C, Huang X, Bayram O, Schinke J, Stumpf S, Dubiel W, Braus GH (2013). Control of multicellular development by the physically interacting deneddylases DEN1/DenA and COP9 signalosome. PLoS Genet 9, e1003275.

Cianfrocco MA, DeSantis ME, Leschziner AE, Reck-Peterson SL (2015). Mechanism and regulation of cytoplasmic dynein. Annu Rev Cell Dev Biol 31, 83–108.

Cioni J-M, Lin JQ, Holtermann AV, Koppers M, Jakobs MAH, Azizi A, Turner-Bridger B, Shigeoka T, Franze K, Harris WA, *et al.* (2019). Late endosomes act as mRNA translation platforms and sustain mitochondria in axons. Cell 176, 56–72.e15.

Cross JA, Dodding MP (2019). Motor-cargo adaptors at the organelle-cytoskeleton interface. Curr Opin Cell Biol 59, 16–23.

Downes DJ, Chonofsky M, Tan K, Pfannenstiel BT, Reck-Peterson SL, Todd RB (2014). Characterization of the mutagenic spectrum of 4-nitroquinoline 1-oxide (4-NQO) in *Aspergillus nidulans* by whole genome sequencing. G3 (Bethesda) 4, 2483–2492.

Egan MJ, McClintock MA, Reck-Peterson SL (2012a). Microtubule-based transport in filamentous fungi. Curr Opin Microbiol 15, 637–645.

Egan MJ, Tan K, Reck-Peterson SL (2012b). Lis1 is an initiation factor for dynein-driven organelle transport. J Cell Biol 197, 971–982.

Fu M, Holzbaur ELF (2014). Integrated regulation of motor-driven organelle transport by scaffolding proteins. Trends Cell Biol 24, 564–574.

Gibson DG, Young L, Chuang R-Y, Venter JC, Hutchison CA, Smith HO (2009). Enzymatic assembly of DNA molecules up to several hundred kilobases. Nat Methods 6, 343–345.

Göhre V, Vollmeister E, Bölker M, Feldbrügge M (2012). Microtubule-dependent membrane dynamics in *Ustilago maydis*: Trafficking and function of Rab5a-positive endosomes. Commun Integr Biol 5, 485–490.

Guimaraes SC, Schuster M, Bielska E, Dagdas G, Kilaru S, Meadows BRA, Schrader M, Steinberg G (2015). Peroxisomes, lipid droplets, and endoplasmic reticulum "hitchhike" on motile early endosomes. J Cell Biol 211, 945–954.

Guo X, Farías GG, Mattera R, Bonifacino JS (2016). Rab5 and its effector FHF contribute to neuronal polarity through dynein-dependent retrieval of somatodendritic proteins from the axon. Proc Natl Acad Sci USA 113, E5318–E5327.

Guo Y, Li D, Zhang S, Yang Y, Liu J-J, Wang X, Liu C, Milkie DE, Moore RP, Tulu US, *et al.* (2018). Visualizing intracellular organelle and cytoskeletal interactions at nanoscale resolution on millisecond timescales. Cell 175, 1430–1442.

Haag C, Steuten B, Feldbrügge M (2015). Membrane-coupled mRNA trafficking in fungi. Annu Rev Microbiol 69, 265–281.

Higuchi Y, Ashwin P, Roger Y, Steinberg G (2014). Early endosome motility spatially organizes polysome distribution. J Cell Biol 204, 343–357.

Hirokawa N, Noda Y, Tanaka Y, Niwa S (2009). Kinesin superfamily motor proteins and intracellular transport. Nat Rev Mol Cell Biol 10, 682–696.

Hoogenraad CC, Akhmanova A (2016). Bicaudal D family of motor adaptors: linking dynein motility to cargo binding. Trends Cell Biol 26, 327–340.
Jansen R-P, Niessing D, Baumann S, Feldbrügge M (2014). mRNA transport meets membrane traffic. Trends Genet 30, 408–417.
Jedd G, Chua N-H (2000). A new self-assembled peroxisomal vesicle required for efficient resealing of the plasma membrane. Nat Cell Biol 2, 226–231.
Kendrick AA, Dickey AM, Redwine WB, Tran PT, Vaites LP, Dzieciatkowska M, Harper JW, Reck-Peterson SL (2019). Hook3 is a scaffold for the opposite-polarity microtubule-based motors cytoplasmic dynein-1 and KIF1C. J Cell Biol 218, 2982–3001.
Lee SB, Taylor JW (1990). Isolation of DNA from fungal mycelia and single spores. In: PCR Protocols, Elsevier, 282–287.
Lenz JH, Schuchardt I, Straube A, Steinberg G (2006). A dynein loading zone for retrograde endosome motility at microtubule plus-ends. EMBO J 25, 2275–2286.
Liao Y-C, Fernandopulle MS, Wang G, Choi H, Hao L, Drerup CM, Patel R, Qamar S, Nixon-Abell J, Shen Y, *et al*. (2019). RNA granules hitchhike on lysosomes for long-distance transport, using annexin A11 as a molecular tether. Cell 179, 147–164.e20.
Lin C, Schuster M, Guimaraes SC, Ashwin P, Schrader M, Metz J, Hacker C, Gurr SJ, Steinberg G (2016). Active diffusion and microtubule-based transport oppose myosin forces to position organelles in cells. Nat Commun 7, 11814.
Markham P, Collinge AJ (1987). Woronin bodies of filamentous fungi. FEMS Microbiol Lett 46, 1–11.
Mogre SS, Christensen JR, Niman CS, Reck-Peterson SL, Koslover EF (2020). Hitching a ride: mechanics of transport initiation through linker-mediated hitchhiking. Biophys J 118, 1357–1369.
Morris NR (1975). Mitotic mutants of *Aspergillus nidulans*. Genet Res 26, 237–254.
Nayak T, Szewczyk E, Oakley CE, Osmani A, Ukil L, Murray SL, Hynes MJ, Osmani SA, Oakley BR (2006). A versatile and efficient gene-targeting system for *Aspergillus nidulans*. Genetics 172, 1557–1566.
Peñalva MA, Galindo A, Abenza JF, Pinar M, Calcagno-Pizarelli AM, Arst HN, Pantazopoulou A (2012). Searching for gold beyond mitosis: mining intracellular membrane traffic in *Aspergillus nidulans*. Cell Logist 2, 2–14.
Pinar M, Pantazopoulou A, Peñalva MA (2013). Live-cell imaging of *Aspergillus nidulans* autophagy: RAB1 dependence, Golgi independence and ER involvement. Autophagy 9, 1024–1043.
Pohlmann T, Baumann S, Haag C, Albrecht M, Feldbrügge M (2015). A FYVE zinc finger domain protein specifically links mRNA transport to endosome trafficking. ELife 4, e06041.
Reck-Peterson SL, Redwine WB, Vale RD, Carter AP (2018). The cytoplasmic dynein transport machinery and its many cargoes. Nat Rev Mol Cell Biol 19, 382–398.
Salogiannis J, Egan MJ, Reck-Peterson SL (2016). Peroxisomes move by hitchhiking on early endosomes using the novel linker protein PxdA. J Cell Biol 212, 289–296.
Salogiannis J, Reck-Peterson SL (2017). Hitchhiking: a non-canonical mode of microtubule-based transport. Trends Cell Biol 27, 141–150.
Schinke J, Kolog Gulko M, Christmann M, Valerius O, Stumpf SK, Stirz M, Braus GH (2016). The DenA/DEN1 interacting phosphatase DipA controls septa positioning and phosphorylation-dependent stability of cytoplasmatic DenA/DEN1 during fungal development. PLoS Genet 12, e1005949.
Shcherbo D, Murphy CS, Ermakova GV, Solovieva EA, Chepurnykh TV, Shcheglov AS, Verkhusha VV, Pletnev VZ, Hazelwood KL, Roche PM, *et al*. (2009). Far-red fluorescent tags for protein imaging in living tissues. Biochem J 418, 567–574.
Shevchenko A, Wilm M, Vorm O, Mann M (1996). Mass spectrometric sequencing of proteins silver-stained polyacrylamide gels. Anal Chem 68, 850–858.
Siddiqui N, Zwetsloot AJ, Bachmann A, Roth D, Hussain H, Brandt J, Kaverina I, Straube A (2019). PTPN21 and Hook3 relieve KIF1C autoinhibition and activate intracellular transport. Nat Commun 10, 2693.
Spits M, Heesterbeek IT, Voortman LM, Akkermans JJ, Wijdeven RH, Cabukusta B, Neefjes J (2021). Mobile late endosomes modulate peripheral endoplasmic reticulum network architecture.. EMBO Rep, e50815.
Splinter D, Tanenbaum ME, Lindqvist A, Jaarsma D, Flotho A, Yu KL, Grigoriev I, Engelsma D, Haasdijk ED, Keijzer N, *et al*. (2010). Bicaudal D2, dynein, and kinesin-1 associate with nuclear pore complexes and regulate centrosome and nuclear positioning during mitotic entry. PLoS Biol 8, e1000350.
Steinberg G (2016). The mechanism of peroxisome motility in filamentous fungi. Fungal Genetics Biol 97, 33–35.
Steinberg G, Harmer NJ, Schuster M, Kilaru S (2017). Woronin body-based sealing of septal pores. Fungal Genetics Biol 109, 53–55.
Straubinger B, Straubinger E, Wirsel S, Turgeon G, Yoder O (1992). Versatile fungal transformation vectors carrying the selectable bar gene of *Streptomyces hygroscopicus*. Fungal Genetics Newsletter 39, 82–83.
Subach OM, Gundorov IS, Yoshimura M, Subach FV, Zhang J, Grüenwald D, Souslova EA, Chudakov DM, Verkhusha VV (2008). Conversion of red fluorescent protein into a bright blue probe. Chem Biol 15, 1116–1124.
Suresh S, Abdurehman L, Osmani AH, Osmani SA (2017). Tools for retargeting proteins within *Aspergillus nidulans*. PLoS One 12, e0189077.
Szewczyk E, Nayak T, Oakley CE, Edgerton H, Xiong Y, Taheri-Talesh N, Osmani SA, Oakley BR, Oakley B (2006). Fusion PCR and gene targeting in *Aspergillus nidulans*. Nat Protoc 1, 3111–3120.
Tan K, Roberts AJ, Chonofsky M, Egan MJ, Reck-Peterson SL (2014). A microscopy-based screen employing multiplex genome sequencing identifies cargo-specific requirements for dynein velocity. Mol Biol Cell 25, 669–678.
Todd RB, Davis MA, Hynes MJ (2007). Genetic manipulation of *Aspergillus nidulans*: meiotic progeny for genetic analysis and strain construction. Nat Protoc 2, 811–821.
Vale RD (2003). The molecular motor toolbox for intracellular transport. Cell 112, 467–480.
Wedlich-Söldner R, Straube A, Friedrich MW, Steinberg G (2002). A balance of KIF1A-like kinesin and dynein organizes early endosomes in the fungus *Ustilago maydis*. EMBO J 21, 2946–2957.
Xiang X, Beckwith SM, Morris NR (1994). Cytoplasmic dynein is involved in nuclear migration in *Aspergillus nidulans*. Proc Natl Acad Sci USA 91, 2100–2104.
Xiang X, Zuo W, Efimov VP, Morris NR (1999). Isolation of a new set of *Aspergillus nidulans* mutants defective in nuclear migration. Curr Genet 35, 626–630.
Xu L, Sowa ME, Chen J, Li X, Gygi SP, Harper JW (2008). An FTS/Hook/p107(FHIP) complex interacts with and promotes endosomal clustering by the homotypic vacuolar protein sorting complex. Mol Biol Cell 19, 5059–5071.
Yao X, Arst HN, Wang X, Xiang X (2015). Discovery of a vezatin-like protein for dynein-mediated early endosome transport. Mol Biol Cell 26, 3816–3827.
Yao X, Wang X, Xiang X (2014). FHIP and FTS proteins are critical for dynein-mediated transport of early endosomes in *Aspergillus*. Mol Biol Cell 25, 2181–2189.
Zekert N, Fischer R (2009). The *Aspergillus nidulans* kinesin-3 UncA motor moves vesicles along a subpopulation of microtubules. Mol Biol Cell 20, 673–684.
Zhang J, Qiu R, Arst HN, Peñalva MA, Xiang X (2014). HookA is a novel dynein-early endosome linker critical for cargo movement in vivo. J Cell Biol 204, 1009–1026.